








Modeling Plasmonic Antennas for the Millimeterwave & THz Range

Hande Ibili , Graduate Student Member, IEEE, Tobias Blatter , Michael Baumann , Laurenz Kulmer , Boris Vukovic , Jasmin Smajic , Senior Member, IEEE, and Juerg Leuthold , Fellow, IEEE

(Invited Paper)

Abstract—Plasmonic modulator antennas have been recently shown to be able to efficiently upmix millimeter and THz waves onto optical frequencies. In this article, we introduce a theory and equivalent circuit models for designing and optimizing plasmonic modulator antennas. The proposed model aims to improve the overall understanding of the experimentally found powerful antenna field enhancement (between the impinging field at the antenna and the field within the modulator). This enhancement has already been shown to be as high as 90'000 and allows to efficiently evaluate relevant figures of merit for antenna design and optimization. The effects of antenna design parameters are presented and discussed in detail. The accuracy of the suggested models is verified by rigorous numerical computation through field simulations. As a result, we propose optimized antenna structures and their parameters, and demonstrate their field enhancement capabilities.

Index Terms—Electro-optic devices, THz antennas, plasmonics, field simulations, equivalent circuit model, THz frequency, and wireless communications.

I. INTRODUCTION

MILLIMETER-WAVE and THz antennas are essential for next-generation wireless communication systems and novel sensing applications. The ideal antennas should offer broadband reception, as well as high gain in the millimeter-wave and THz range. In addition, they are expected to be sensitive, compact, and monolithically integrable with standard silicon fabrication lines. Towards this goal, current complex and comparably high-cost conventional RF electronic components with amplification and mixing stages may be replaced by schemes that employ direct mixing of THz waves to the optical domain. This way, higher data transfer rates and lower power consumption at higher speeds can be achieved.

Manuscript received 3 March 2023; revised 31 August 2023; accepted 8 September 2023. Date of publication 12 September 2023; date of current version 6 October 2023. This work was supported by Innosuisse–Swiss Innovation Agency in the frame of the Innovation Project No. 53099.1 IP-ICT “Ultra-Miniature Wideband 5G & 6G Electromagnetic Radiation Sensor (5&6-GEARS)”. (Corresponding author: Jasmin Smajic.)

The authors are with the Institute of Electromagnetic Fields, ETH Zurich, 8092 Zurich, Switzerland (e-mail: hande.ibili@ief.ee.ethz.ch; tobias.blatter@ief.ee.ethz.ch; michael.baumann@ief.ee.ethz.ch; laurenz.kulmer@ief.ee.ethz.ch; boris.vukovic@ief.ee.ethz.ch; jasmin.smajic@ief.ee.ethz.ch; juerg.leuthold@ief.ee.ethz.ch).

Color versions of one or more figures in this article are available at <https://doi.org/10.1109/JSTQE.2023.3314696>.

Digital Object Identifier 10.1109/JSTQE.2023.3314696

Direct RF-to-optical conversion has been a topic for the past 30 years [1], [2]. Traditional approaches [3] are based on receiving an RF signal in an antenna, amplifying the electrical signal and then forwarding it to a modulator, where the electrical signal is mapped onto an optical carrier. Over the years, the community came up with more compact integrated schemes. For instance, a patch antenna was embedded in a lithium tantalate substrate. There was a narrow gap and a straight optical waveguide located under the gap to convert microwaves to light waves [4]. In another instance, an antenna was directly connected to a silicon-based slow-light modulator [5]. However, conversion efficiencies were rather low, as the electro-optic (EO) effect is rather weak. Other implementations of antenna-embedded modulators with EO polymer waveguides or connected dielectric antennas to whispering gallery mode resonators have been reported [6], [7], [8], [9]. These structures suffer from having a narrow frequency response limited by the bandwidth of the optical modulator and low conversion efficiencies.

To overcome the modulator speed limitations and improve the efficiency, a novel concept exploiting a plasmonic electro-optical modulator structure with an integrated antenna has been proposed [10]. Benefiting from its subwavelength confinement abilities, the plasmonic approach is a viable solution for direct THz to optical conversion [11] with high sensitivity (with field enhancement values of 100 dB [12]) and smaller footprints [11], [12].

However, an important question remains: How to design a most efficient on-chip plasmonic millimeter-wave and THz antenna with embedded modulators? Modeling classical [13] or THz antennas [14] is typically based on equivalent circuit analysis [15], [16], [17], [18], [19], [20], [21], [22] and is well established in the literature. Our proposed model incorporates frequency-dependent parameters, all while preserving the simplicity of our circuit design. That being said, the above-mentioned plasmonic antennas differ from classical antenna theory in several ways. First, they do not possess a feed network like traditional antennas. Second, they are composed of a plasmonic EO modulator and antenna parts. A methodology is thus needed that provides insight into the effects of design parameters on the performance of millimeter-wave and THz plasmonic antennas. In [10], an analytical expression has been introduced that provides an understanding of the field enhancement mechanisms that can be achieved with the plasmonic antenna approach.

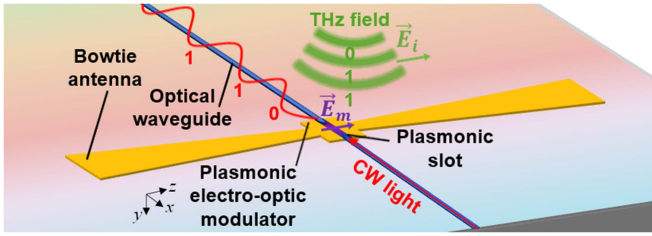


Fig. 1. Concept of plasmonic modulator antenna is illustrated. The antenna captures incoming THz radiation which is then intensified at the plasmonic slot.

And indeed, field enhancement values in the order of 90'000 have already been shown [12]. Other studies on the optimum geometry for obtaining broadband or largest field enhancements include [20], [23], [24], [25], [26], [27].

In this article, we provide a modeling method and a path to identify the ideal modulator antenna geometry for converting millimeter- and THz waves to the optical domain at highest efficiency. Finding the ideal solution is a challenge as the antenna and the modulator part are strongly coupled. Insight into the physics is given by analytical expressions based on equivalent circuit modeling. The results are verified by full-wave field simulations. In this work, we exclude any effects of the cladding or surrounding materials, but rather focus on the physics of the antenna with the modulator.

This article is organized as follows: In Section II, the concept of the plasmonic modulator antenna is described. Section III follows with the theory of the proposed method explained in detail. Section IV showcases the effects of the plasmonic antenna parameters. Section V presents the numerical results for realistic plasmonic modulator antenna devices. Finally, the conclusion and outlook are given in Section VI.

II. PLASMONIC MODULATOR ANTENNA CONCEPT

The device under consideration is depicted in Fig. 1. The design follows the study in [10]. Such devices consist of two components: a plasmonic electro-optic modulator and an antenna section. Here, an incident THz field E_i is received by an antenna and translated to an electrical field E_m across a plasmonic slot, where it is used in an electro-optical modulator to encode the information onto an optical continuous wave (CW) signal. The ultimate design goal for the antenna and modulator is to enhance the field E_m with respect to E_i .

Plasmonic electro-optic modulators are of interest for mapping an electrical signal onto the optical domain. The plasmonic modulators are the only modulators that offer bandwidths in excess of 500 GHz [28], [29], [30]. The operation principle has been described in [31], [32]. A continuous-wave optical signal is fed through an optical waveguide to a plasmonic slot. The plasmonic slot consists of an organic [33] or inorganic [34] electro-optic material in its center and metallic walls at the side. The metallic walls not only form the plasmonic waveguide, but also act as RF electrodes. Upon the application of a field on the electrodes, the refractive index of the electro-optic material within the slot experiences a change. Thereby, the electrical signal is encoded onto the optical signal. Typical slot widths are

in the order of 100 nm and typical lengths are in the order of a few micrometers [32]. The high confinement of the plasmonic mode and the large field enhancement within the gap provide a high modulation efficiency. The small dimensions of the modulator and the utilization of the Pockels-effect for nonlinear switching in the slot guarantee an ultra-fast response.

The antenna section is an extension of the electrodes [10]. The antenna can have any shape. It might e.g., have the form of a simple dipole [10], a four-leaf-clover (FLC) [12], or a bowtie [35] shape as depicted above in Fig. 1 being planar, i.e., suitable for on-chip manufacturing.

The advantages of on-chip plasmonic modulator antenna-based devices are manifold [10], [11], [12]: 1) High RF losses and electromagnetic interference issues introduced by conventional RF to optical conversion systems are eliminated; 2) They offer broad bandwidths at highest carrier frequencies. These high bandwidths have their origin in the facts that the modulators rely on the fast Pockels effect, they are extremely compact and therefore only have a small RC-constant; 3) Detection of weak fields at higher frequencies is possible. This is because the antenna comes with built-in field enhancement up to 100 dB [12]; 4) Miniaturized and compact devices can be envisioned; 5) Lastly, the devices are compatible with standard silicon fabrication methods.

III. THZ-ANTENNA MODELING AND SIMULATIONS

In this section, we introduce the theoretical framework for modeling the plasmonic antennas based on an equivalent circuit theory and field simulations.

Designing antennas with the help of field simulation tools is well established and widely used [36], [37], [38], [39], [40]. This field-simulation approach typically involves modeling a lumped port or a waveguide port within the antenna's feeding subdomain through which the simulation model is connected to an electronic circuit. The antenna is surrounded by a spherical free-space domain large enough for the near-field distribution of the antenna and its transition to the radiating field. The surrounding air region is terminated by an appropriate absorbing boundary condition (ABC) [41]. The antenna parameters, such as radiation pattern and directivity, are obtained by solving the E-field wave equation in the frequency domain for a given excitation at the input lumped port. The electromagnetic field over the lumped port is then integrated to be used for obtaining the antenna impedance and S-parameters (given a reference or characteristic impedance). These classical design parameters are essential for matching the impedances of the electronics to the antenna in order to maximize antenna's efficiency [42].

Antenna-coupled modulators, as shown in Fig. 1, vary from classical RF antennas in several important aspects: They neither have a feeding port nor an electronic circuit to be attached to. This fundamentally deviates from classical RF antenna designs, where the power coupling into a transmission line is usually maximized. In contrast, for the antenna-coupled modulators, the goal is to maximize the electric field across the modulator.

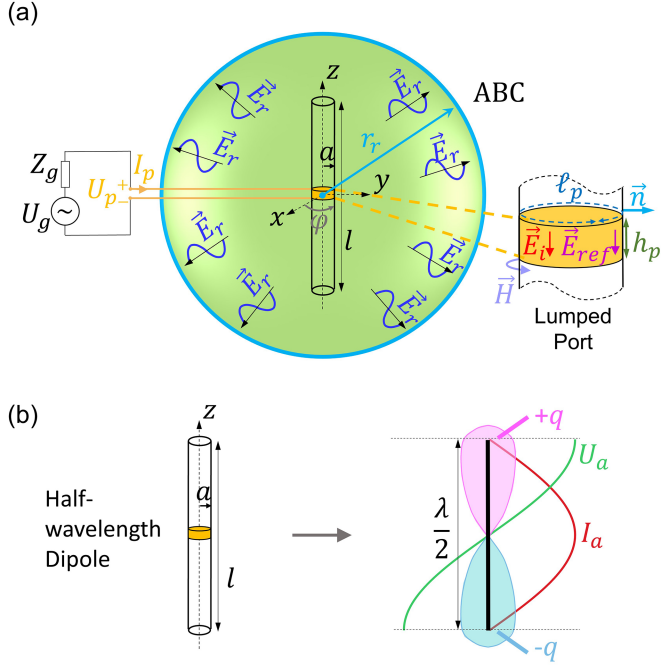


Fig. 2. Reference dipole antenna with lumped port feeding. (a) Antenna geometry, its connection with a signal source (generator voltage U_g , impedance Z_g), lumped port details (height h_p , circumference l_p), port incident field E_i , scattered field at the port E_{ref} , total magnetic field H , radiated field characterized by E_r and H_r , and (b) current I_a , voltage U_a and charge density $\pm q$ (blue and pink shaded area) distributions over the half-wavelength dipole antenna are depicted. More details can be found in the text.

One could think that simulating the antenna-coupled modulator from Fig. 1 can simply be divided into two subproblems, namely the optimization of the THz antenna and the electro-optic modulator. However, changing one influences the other and hence, simultaneous and combined investigation of the two is needed. Subsequently, we present the required theory and modeling approach for designing THz antennas for EO modulators.

Below, we will introduce a method to simulate plasmonic modulator antennas and validate this method. Regarding the complexity of our method, we start with a reference transmission antenna and calculate its impedance Z_p . We then use our own method (which operates in reception mode) to derive the antenna impedance Z_a . Ideally, the two impedances should be identical. More precisely, we will proceed as follows: A) First, we will introduce a half-wavelength dipole antenna with traditional lumped port excitation. For this antenna, we will find the antenna impedance Z_p ; B) As a second step, we will continue with the half-wavelength dipole antenna with external excitation. We will find the equivalent circuit for this antenna. The impedance Z_a of the antenna equivalent circuit will then be compared against the lumped port impedance; the agreement of both impedances $Z_a \cong Z_p$ verifies the model. Once the concept and theoretical framework are elaborated, we will move on to (C) and simulate a full-wavelength dipole antenna, using the equivalent circuit model from above and complement it with the capacitance of the EO modulator by utilizing the proposed method. Our results are obtained by using commercially available COMSOL vector

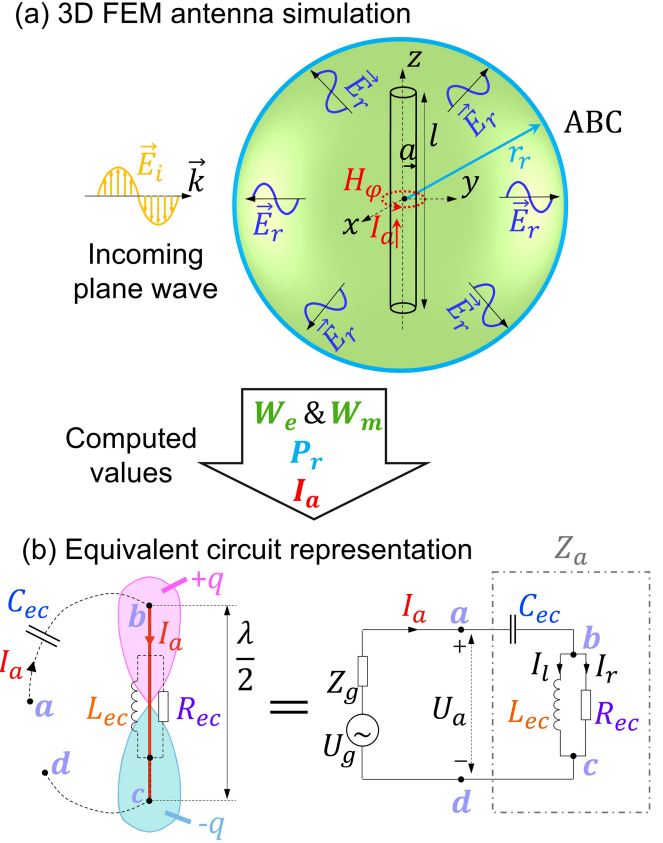


Fig. 3. (a) Proposed analysis of THz antennas with a plane-wave excitation by using 3-D FEM simulations is shown. The dipole antenna defined in Fig. 2(a) is modeled without a lumped port, i.e., without the feeding sub-region. The antenna is surrounded by a spherical free space terminated by an ABC. The radius of the surrounding space should be at least three wavelengths long to assure the far field conditions. Considering the distribution of the antenna charge, voltage, and current, a simplified equivalent circuit of the antenna is defined. (b) Representation of the equivalent circuit for the half-wavelength dipole antenna. The computed values are utilized to derive the equivalent circuit parameters. More details can be found in the text.

finite element method (FEM) solver. This solver computes directly the field in the model without the need for computationally expensive post processing stage. The typical number of linear elements used is around 5 million resulting in a similar number of degrees of freedom. A modern parallel version of a direct linear solver called PARDISO was used for the presented simulations. The computation of a single frequency solution takes around 20 mins on a modern computing multicore hardware (Intel Xeon CPU E5, 2.4 GHZ, 8 cores, 128 GB RAM).

A. Traditional Lumped-Port Approach

First, as a reference case for verification purposes, a cylindrical dipole antenna of length $l = \lambda_{RF} / 2$ and radius a , presented in Fig. 2(a) is chosen. This antenna is modeled according to the described common practice with a lumped port. For the sake of completeness, it is worth writing the following lumped port boundary condition [41]. More details can be found

in Appendix A.

$$\begin{aligned} \vec{n} \times \left(\frac{1}{\mu} \nabla \times \vec{E} \right) + \frac{j\omega}{Z_s} \vec{n} \times (\vec{n} \times \vec{E}) \\ = \frac{2j\omega}{Z_s} \vec{n} \times (\vec{n} \times \vec{E}_i) \end{aligned} \quad (1)$$

$$\vec{E} = \vec{E}_i + \vec{E}_{ref} \quad (2)$$

$$Z_p = \frac{U_p}{I_p} = \frac{\int_{h_p} \vec{E} \cdot d\vec{l}}{\int_{\ell_p} \vec{H} \cdot d\vec{l}} = \frac{E_z h_p}{H_\varphi \ell_p} = Z_s \frac{h_p}{\ell_p}, \quad (3)$$

where \vec{E} is the total electric field (computed by FEM) across the port, \vec{E}_i is the incident electric field (produced by the applied generator voltage), \vec{E}_{ref} is the scattered electric field at the port, \vec{H} is the total magnetic field at the port, \vec{n} is the normal unit vector to the port surface, ω is the source angular frequency, $\mu = \mu_0 \mu_r$ is the magnetic permeability of the port material, Z_s is the port surface impedance (the ratio between the electric and magnetic field within the port), Z_p is the lumped port impedance (the ratio between the port voltage and current), U_p is the produced port voltage (U_g is the input voltage of the source by the user), I_p is the port current, h_p is the port height, and $\ell_p = 2\pi a$ is the port width. In (3), it is described that the port voltage is obtained by integrating the total electric field over the port height and, similarly, the port current is obtained by integrating the total magnetic field over the width ℓ_p of the port (Ampere's law).

In order to get an idea of the antenna parameters, we now perform a 3-D vector FEM simulation in the frequency domain for an exemplary geometry. In this example, the excitation of the antenna is realized by applying a voltage source with $U_g = 1$ V and $Z_g = 50 \Omega$ through the lumped port of Fig. 2(a). The antenna is designed for a frequency $f_{RF} = 200$ GHz, i.e., a wavelength $\lambda_{RF} = 1499 \mu\text{m}$ with a wire radius $a = 1.099 \mu\text{m}$, a port height $h_p = 1 \mu\text{m}$, and an antenna length $l = \lambda_{RF}/2$. The voltage U_a , the current I_a , and charge distribution $\pm q$ over the half-wavelength dipole are also illustrated in Fig. 2(b). The distribution of electrical current and voltage over an antenna is driven by the accumulation of opposing electrical charges. The two ends of the antenna, referred to as open circuits, act as points of zero conduction current flow within the dipole. The current flow is maximized at the middle of the dipole, whereas the voltage (obtained by integrating along the dipole in the electrostatic sense) across the dipole antenna is maximal at the ends of the antenna and decreases to zero at the middle of the antenna. The phase of the voltage across the antenna is also opposite at the two ends, with one end being at the peak of the voltage cycle, and the other end having the opposite signed voltage.

Using the parameters introduced in the previous paragraph, we perform simulations to extract the total electrical field \vec{E} and magnetic field \vec{H} across the port. The obtained fields at the port were then integrated according to (3) and the following antenna impedance was obtained.

$$Z_p = \frac{U_p}{I_p} = R_r + jX_a = 85.45 + j48.79 (\Omega), \quad (4)$$

where, R_r is the radiation resistance, and X_a is the antenna reactance.

It is important to mention that although the length of the antenna has been adjusted to $l = \lambda_{RF}/2$, the antenna reactance is not equal to zero (no pure resonance) due to the fact that the finite thickness of the antenna shifts the resonance slightly to a lower frequency.

Since solution (4) is essential for verifying the proposed theory below, it has been computed with highest possible accuracy guaranteed by rigorous mesh convergence and ABC distance studies.

B. Proposed Method Utilizing Field Simulations and Equivalent Circuit Model

We are now switching to the antenna depicted in Fig. 3(a). This antenna is no longer excited through a source generator (hence short circuited), but by a plane-wave with an incident field \vec{E}_i . The antenna impedance, Z_a , could be derived by means of a 3-D FEM simulation as before. Yet, the contributions of the capacitive, the inductive and the resistive parts would still be uncertain. These parameters will later guide us in designing the best antenna. For this, we need to find the parameters of the equivalent circuit in Fig. 3(b). The topology of the equivalent circuit is defined by the behavior of the antenna under the applied excitation. The electric near field of the antenna is distributed between its opposite ends, where the charge density has its maximum value. This charge accumulation at the ends of the antenna introduces the equivalent antenna capacitance, see Fig. 3(b). Additionally, the antenna current flowing through the wire leads to the inclusion of the antenna inductance L_{ec} and the antenna resistance R_{ec} in the equivalent circuit as a parallel combination, see Fig. 3(b). This equivalent circuit is subsequently needed for the interaction study of the antenna with the modulator capacitance.

The challenge with finding the respective R_{ec} , C_{ec} and L_{ec} is that the conventional lumped-port FEM simulation, at best, provides a single parameter (antenna impedance, Z_a) for these three unknowns. The idea to derive these parameters employs the antenna current, the time-average electric and magnetic energies, as well as the radiated power as obtained through a 3-D FEM simulation.

As a first step, we use the 3-D FEM simulations and electromagnetic scattering theory to derive the radiated fields. The antenna structure is modeled in a computational domain that includes a spherical air region of sufficient size to ensure that the far-field conditions are met. The simulation employs a plane-wave excitation, and an ABC is applied to terminate the domain properly. We then calculate the radiated power of the antenna (P_r) on the surface of the air domain, the time-average electric (W_e) and magnetic (W_m) energies of the scattered field (removing the incident field) over the air domain, and the antenna current (I_a). These values are then used to find the equivalent circuit parameters of the antenna.

The energy scattered from the antenna through the outer surface of the surrounding space (W_r) is obtained from the time average Poynting vector flux (radiated power). The time-average

electric (W_e) and magnetic (W_m) energies of the field within the surrounding space are obtained by integrating the scattered E_r and H_r field. The antenna current I_a is obtained by integrating the magnetic field H_φ over a circular path in the middle of the antenna (Ampere's law).

Caution needs to be taken for deriving the radiated energy. In the vicinity of the antenna, the electromagnetic field comprises both the radiating and the induction fields. The energy of the radiated field distributed around the antenna, W_r , is therefore obtained by multiplying the radiated power in the far field, P_r , and the propagation time from the antenna to the surface enclosing the computational domain (ABC).

$$W_r = P_r \frac{r_{sc}}{v}, \quad v = \frac{1}{\sqrt{\mu\varepsilon}}, \quad (5)$$

where r_{sc} is the far field radius of the surrounding spherical air domain, v is the speed of light in air.

The energy of the radiated field, W_r , is equally distributed between the electric and magnetic fields. Thus, subtracting half of the radiated energy from each of the total electric and magnetic energies yields the corresponding near-field induction energies W_e^{near} and W_m^{near} :

$$W_e^{near} = W_e - \frac{1}{2}W_r \quad (6)$$

$$W_m^{near} = W_m - \frac{1}{2}W_r. \quad (7)$$

These time-averaged near-field energies (6) and (7) determine the equivalent antenna capacitance and inductance, respectively. To complete the equivalent circuit model, the relation of the antenna resistance with the computed values is required. The calculations of the equivalent circuit parameters can be mathematically presented as follows. Details of which can be found in Appendix B.

$$R_{ec} = \frac{2(P_r^2 + \omega^2 W_e^{near2})}{P_r I_a^2} \quad (8)$$

$$L_{ec} = R_{ec} \frac{P_r}{\omega^2 W_m^{near}} \quad (9)$$

$$C_{ec} = \frac{I_a^2}{2\omega^2 W_e^{near}} \quad (10)$$

Equations (8)–(10) are results of the circuit analysis, see Fig. 3(b). They provide a set of relationships between the different components of the equivalent circuit. They have been derived from a voltage- and a current-circuit-equation (Kirchhoff's laws) and by taking into account the available far-field time-average radiating power and time-average electric and magnetic near-field energies.

In order to obtain the equivalent circuit parameters, we perform the 3-D FEM simulation for the half-wavelength dipole without a lumped port; thereby, without a gap in the middle of the dipole (short circuited), see Fig. 3(a). To this end, a plane wave excitation propagating in the y -direction with a z -polarized E-field of $E_i = 5$ V/m is applied. The resulting electric and magnetic near-field distribution plots are depicted in Fig. 4. The electric field distribution is related to the charges, and it reveals a charge concentration. Likewise, the magnetic field

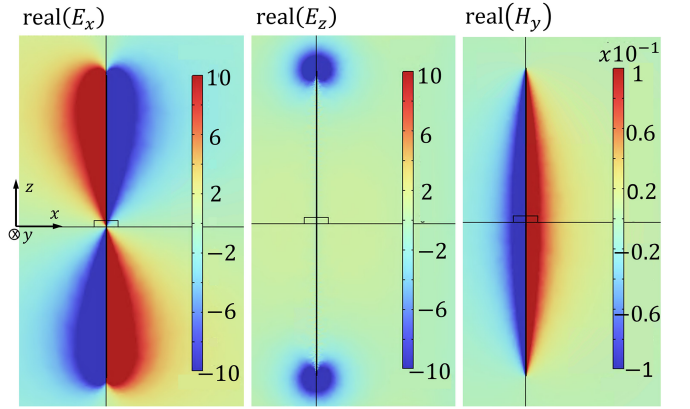


Fig. 4. Resulting electric and magnetic near-field distributions of the reference dipole antenna at 200 GHz are presented.

TABLE I
EQUIVALENT CIRCUIT PARAMETERS OF THE HALF-WAVELENGTH DIPOLE

PARAMETER	VALUE	UNIT
I_a	25.72489	μA
U_g	11.84424	mV
R_g	376.82	Ω
U_a	2.48872	mV
C_{ec}	0.64824	fF
R_{ec}	20.48657	k Ω
L_{ec}	1.02365	nH

distribution corresponds to the antenna current, and it shows a maximum in the middle of the antenna. Thereby, Fig. 4 justifies the simplified representation shown in Fig. 2(b). With the aid of the computed fields from the 3-D FEM simulation, we now extract the equivalent circuit parameters, which leads us to the values presented in Table I.

It is worth mentioning that the equivalent resistance R_{ec} in (8) should not be confused with the radiation resistance R_r appearing in (4), as these are related, but two different values. The radiation resistance is the real part of the antenna impedance as stated previously, representing the radiated power, P_r . Since the equivalent resistance is in parallel to the equivalent inductance and both are in series with the equivalent capacitor, the resulting value of the antenna impedance is determined by the overall interaction of these components. The numerical results presented in Table I yield the equivalent circuit antenna impedance,

$$Z_a = \frac{U_a}{I_a} = R_r + jX_a = 80.45 + j53.73 \quad (\Omega). \quad (11)$$

The antenna impedance Z_a in (11) is rather close to the one in (4) obtained by a field simulator with a lumped port excitation. In fact, since the antenna geometry is identical and there should not be any difference between exciting the antenna by applying a voltage U_p across a lumped port or a plane-wave incident field E_i , we expect $Z_p \cong Z_a$. The disagreement of 7% in terms of the absolute impedance value is attributed to an extremely large aspect ratio between the antenna radius (~ 1 μm) and the

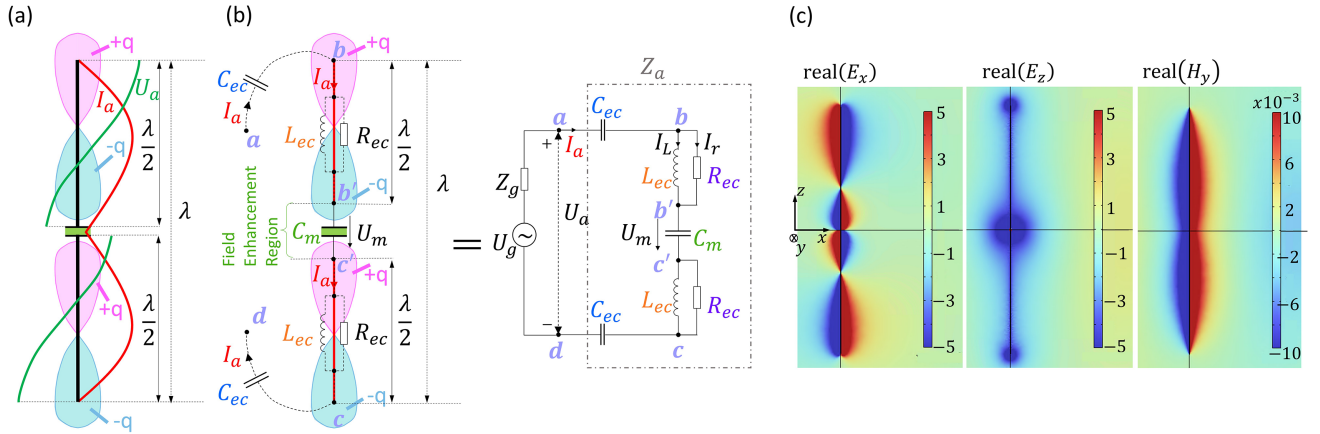


Fig. 5. (a) Current I_a , the voltage U_a and the charge density $\pm q$ (blue and pink shaded area) distributions over the full-wavelength dipole antenna with modulator are depicted. (b) Representation of the equivalent circuit for the plasmonic modulator antennas. For obtaining a high E-field enhancement, a solution based on two $\lambda/2$ antennas separated by an electro-optical modulator is presented. (c) The corresponding near-field distributions of the plasmonic modulator antenna structure are depicted. More details can be found in the text.

antenna length (~ 7.5 mm), resulting in a dense mesh and high computational cost. The agreement of the results is, however, sufficient to confirm the accuracy of the proposed method for evaluating antenna parameters without a feeding lumped port.

C. Plasmonic Antenna With Modulator

We now have the tools and framework to suggest an equivalent circuit of the plasmonic antenna from Fig. 1 and such a circuit is plotted in Fig. 5(b). Conceptually, it is derived from Fig. 3(b) as follows: Two identical antenna equivalent circuits representing the two arms of the plasmonic antenna are separated by a capacitor that acts as a modulator. The presented $\lambda/2$ dipole reference antenna at the considered frequency (200 GHz), by itself, alone would not be sufficient to drive an electro-optical modulator. In a $\lambda/2$ dipole, the electric charge is concentrated at both the antenna ends and no charge exists in the middle of the structure, i.e., around what we previously called the feeding point. Integrating an electro-optical modulator into the feeding region of this antenna would lead to poor field enhancement performance, as the E-field would be rather low due to the charge absence. Hence, a combination of two identical antennas is used to reach the highest field enhancement in the middle of the structure. The modulator is then placed in the middle of the structure, see Fig. 6(a). As an example, a modulator with a slot of $w_{slot} = 1.2 \mu\text{m}$, and an area of $A = d_{mod} l_{mod} = 113 \mu\text{m}^2$, resulting in a capacitance of $C_m = \epsilon_0 A/w_{slot} = 0.834$ fF, is defined, see Fig. 6(a). The antennas connected to each side of the modulator plates provide a field enhancement within the modulator achieved by two opposite electric charge accumulations of these two antennas since they are exposed to the same plane wave excitation, see (a). As the half-wavelength dipole, the plasmonic modulator antenna exhibits zero current flow at its two ends. However, since the modulator capacitor draws current, a non-zero current is anticipated at the middle of the antenna. For the voltage distribution, opposite phases and voltage maxima are expected both at the two ends, as well as at the modulator plates. The numerical results are presented in Fig. 5(c). The mentioned

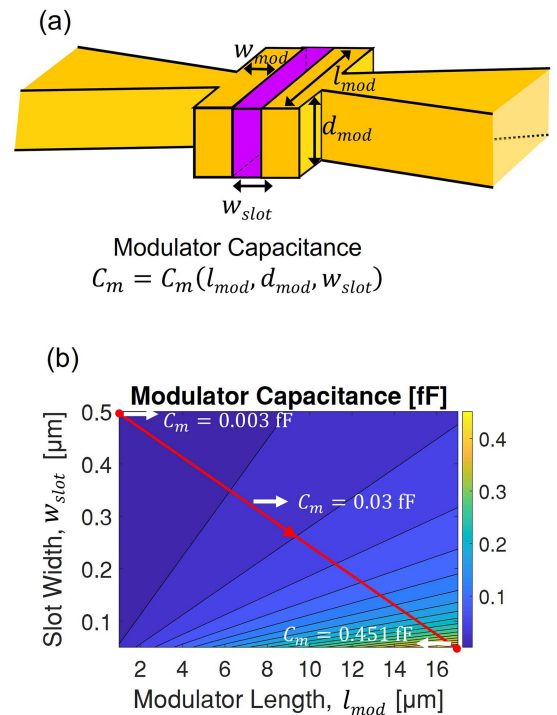


Fig. 6. (a) Geometry details of the modulator capacitance are depicted. (b) Capacitance of the modulator in terms of its geometric parameters.

charge separation is visible and confirmed by the electric near field. Additionally, the electric current flows are recognizable by the H-field plot.

In addition, Fig. 5(c) indicates several important effects: The presence of the modulator considerably changes how the current and charges are distributed within each antenna (compared to an open-circuited dipole). The electric charge concentration on the antenna parts near the modulator is lower than those at the opposite ends, see Fig. 5(c), (left). This is understandable as the modulator consumes the charge due to its electric current. The

TABLE II
EQUIVALENT CIRCUIT PARAMETERS OF THE FULL-WAVELENGTH DIPOLE WITH MODULATOR

PARAMETER	VALUE	UNIT
I_a	8.75445	μA
U_g	6.24427	mV
Z_g	376.82	Ω
U_a	3.25941	mV
C_{ec}	0.45096	fF
R_{ec}	30.26726	k Ω
L_{ec}	1.70753	nH
C_m	0.83109	fF
U_m	8.38243	mV

antenna current distribution is also changed around the modulator, as the current does not have a zero value there, see Fig. 5(c), (right). As aimed, see Fig. 5(c), (middle), high field enhancement values are observed in the middle of the structure. These effects change the distribution of the radiated and near-fields, and lead to modifications of the antenna parameters of a single dipole antenna listed in Table I when compared to the those of the plasmonic antenna listed in Table II. It is evident that each $\lambda/2$ dipole has different parameters as a part of the λ antenna with the modulator. This also evidences that the modulator influences the current and charge distribution of each $\lambda/2$ dipole resulting in their different parameters.

The values of the antenna parameters presented in Fig. 5(b) and Table II provide the following antenna impedance,

$$Z_a = \frac{U_a}{I_a} = R_r + jX_a = 302.71 - j213.74 \ (\Omega). \quad (12)$$

Compared to the impedance in (11), a considerable increase of the impedance due to a series connection of two antennas and the influence of the modulator is evident.

An important aspect of the plasmonic antenna is the field enhancement (FE) between the incoming plane wave E_i and the modulator E-field E_m . The FE in the plasmonic antenna and the equivalent circuit model is calculated via the modulator voltage U_m as follows:

$$\text{FE} = \frac{|E_m|}{|E_i|} = \frac{|U_m|}{|E_i w_{slot}|}, \quad (13)$$

where $U_m = E_m w_{slot}$ is the voltage dropping off across the modulator slot. In the equivalent circuit model, the modulator voltage can be calculated from the simulated I_a and the capacitive impedance by $|U_m| = |I_a| / \omega C_m$.

The result of the equivalent circuit analysis when sweeping the operation frequency from 50 to 250 GHz is shown in Fig. 7. The current responses of the half-wavelength and full-wavelength antennas are plotted in Fig. 7(a). The equivalent circuit values fed into (13) can then be used to derive the FE, see the solid dark blue plot in Fig. 7(b). The FE at 200 GHz is found to be 601. This needs to be compared against a full 3-D FEM simulation, see the dashed light blue line in Fig. 7(b) and a FE at 200 GHz of 596.

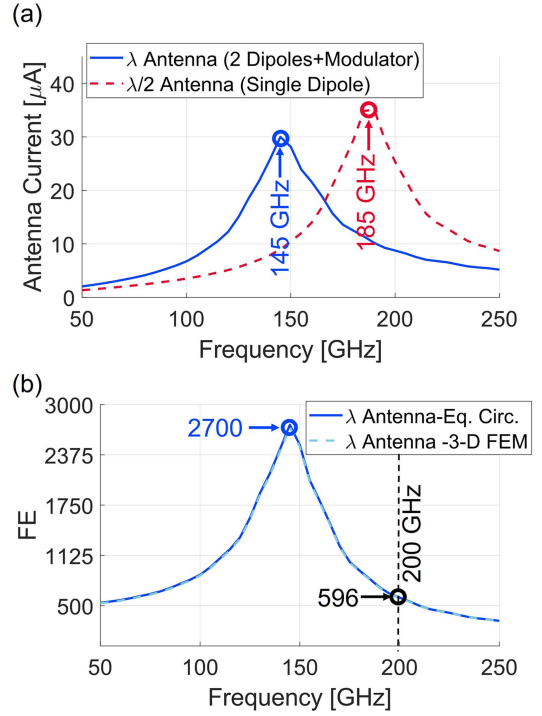


Fig. 7. (a) Resonance shift of the antenna current due to the existence of the modulator is presented. (b) The field enhancement response of the plasmonic antenna with respect to frequency is given.

This shows a very good agreement of the 3-D FEM value with the circuit model with below 1% relative error. Also, this validates the value of C_m and its interaction with the antenna current. Further, along with the impedance simulation, this verifies the entire model.

3-D FEM simulations of antennas for EO modulators are time-consuming and require large memory capacity. They, however, offer an accurate way to extract the parameters of antennas with arbitrary geometry. Once established, the equivalent circuits presented in Figs. 3(b) and 5(b) are useful to perform detailed modulator studies without these computationally intensive 3-D FEM models in the following way: If the modulator is much smaller than the wavelength, only its electrical capacitance influences the antenna parameters. In other words, the antenna behavior is not influenced by single geometric features of the modulator, but only by their overall effect resulting in the modulator capacitance. This enables the decoupling of the modulator from the antenna analysis, shown in Table II.

IV. NUMERICAL PROCEDURE TO DERIVE THE CHARACTERISTICS OF PLASMONIC ANTENNA

In this section, we analyze the effects of the plasmonic modulator within the plasmonic antenna utilizing the theoretical framework described in the previous section. Ultimately, we aim at optimizing the field enhancement. For this, we need to find the optimal set of modulator and antenna parameters.

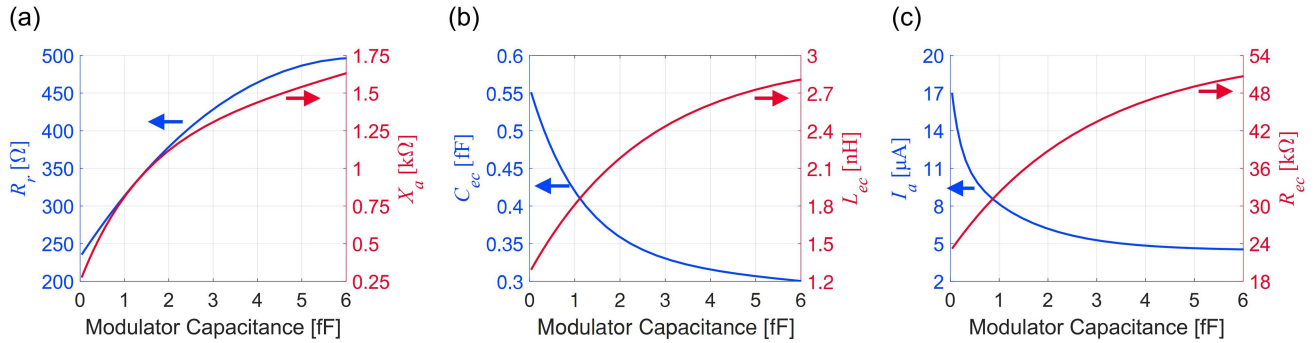


Fig. 8. Numerical results demonstrating the influence of the modulator capacitance over (a) radiation resistance and antenna reactance, (b) equivalent circuit components, antenna capacitance and antenna inductance, and (c) antenna current and antenna resistance are given. It is evident that the modulator capacitance considerably affects the parameters of the adjacent $\lambda/2$ antennas. (Remark: The overall structure is off-resonant).

The modulator geometry and structure could be very complex, containing several parameters, such as the slot width (w_{slot}), modulator length (l_{mod}), thickness (d_{mod}) and also metal width (w_{mod}), see Fig. 6(a). This will result in a multidimensional space within which a search for optimal modulator performance should be performed.

In the first step, we calculate the capacitance of the modulator. This capacitance can be either computed analytically (lower accuracy) or computed by means of 3-D FEM simulations (higher accuracy). For a choice of realistic modulator widths and lengths, one can then find the respective capacitances on the red line in Fig. 6(b). This computationally expensive single parameter (C_m) FEM study enables subsequent multidimensional modulator studies.

In the next step, we perform 3-D FEM simulations at a given frequency $f = 200$ GHz following the procedure described in (7) to (9) in order to extract R_{ec} , C_{ec} , and L_{ec} . The simulations are performed on the whole antenna and for a given range of modulator capacitances (C_m), as found to be of interest in Fig. 6(b). The corresponding results are presented in Fig. 8(a)–(c). The simulations lead to the following interpretation: By increasing the modulator capacitance, the modulator takes more charge from the attached ends of both antennas. This changes the electric near-field energy, consequently changing C_{ec} , as visible in Fig. 8(b). The antenna's current distribution has also been changed, Fig. 8(c), reaching a considerable value, as opposed to a modulator-free $\lambda/2$ case. This changes the energy of the magnetic near-field and causes a change in the equivalent antenna inductance L_{ec} , see Fig. 8(b). The said changes in charge (or C_{ec}) and current distributions (or L_{ec}) considerably affect the antenna's capabilities to send/receive electromagnetic radiation since the antenna is a converter of the standing current and voltage waves along the antenna into a propagating wave around the antenna or vice versa. Ultimately, the goal is to optimize both C_{ec} and L_{ec} such that the radiation i.e., the radiation resistance R_r , hence R_{ec} , is maximized and reactance X_a is minimized within the reachable voltage levels of the voltage source of the circuit. This is also visible in Table III where the correlation between the resistance and field enhancement is evident. Furthermore, reduction of the reactance X_a reduces the corresponding voltage drop across itself, which leads to a

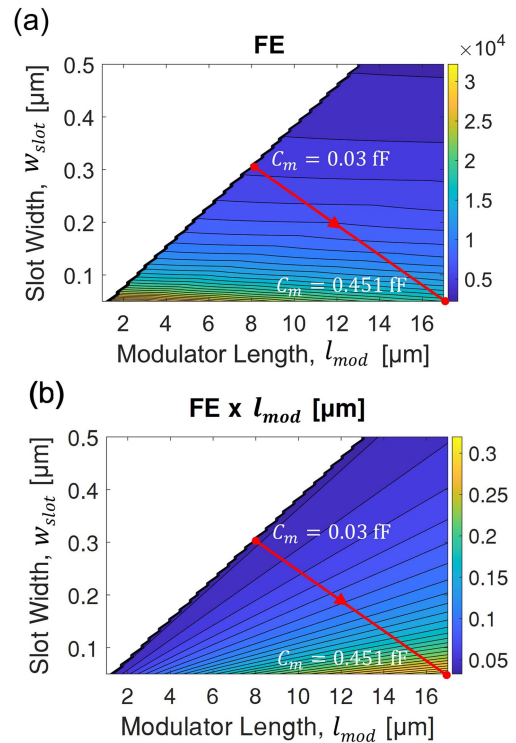


Fig. 9. FE (a) and FOM (b) responses with changing modulator dimensions are presented by our purposed method with decoupling modulator capacitance.

higher voltage across the resistance R_r , i.e., to higher radiated power.

Now that we have all the parameters of the equivalent circuit for different modulator capacitances at $f = 200$ GHz, we can plot the FE, see Fig. 9. It is to be noted that the values in Fig. 9 are off-resonant FEs, as we kept the geometry of the antenna from Fig. 7(b). Also, it is to be noted that the FE changes with the modulator capacitance and the slot width. We, therefore, choose to plot the FE as a function of the modulator length and the slot width. Also, the capacitance values are shown for two points, see Fig. 9(a). It can be seen how the FE grows the smaller the width w_{slot} becomes, whereas the FE decreases with the length of the modulator l_{mod} . The latter should be taken with a word of

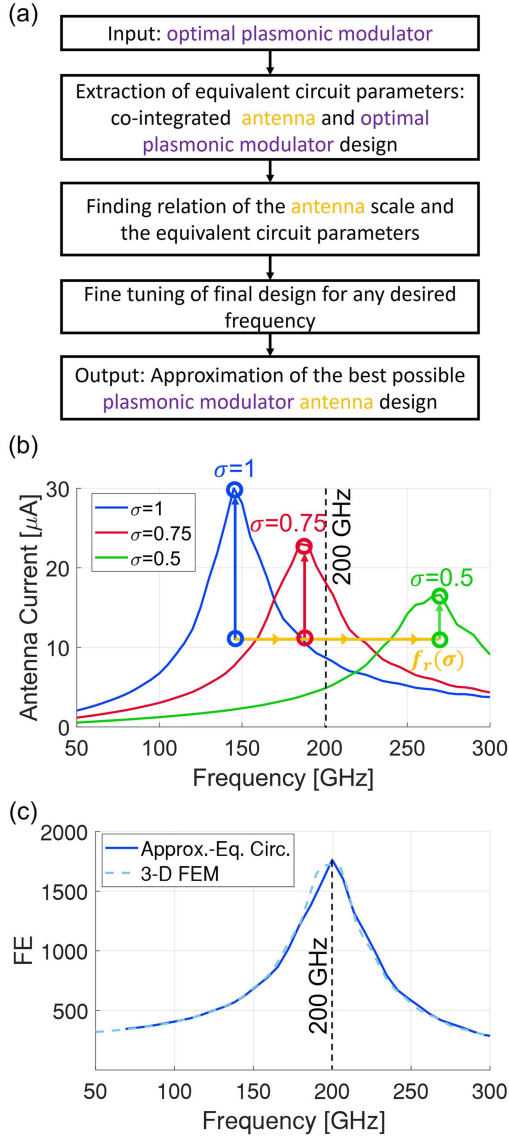


Fig. 10. (a) Flowchart illustrates the systematic process for designing an optimal plasmonic modulator antenna operating at any desired frequency. (b) With the help of 3-D-FEM simulations, the antenna current results for three different antenna sizes (scaling factors σ) with respect to frequency are obtained. This is then needed to extract the equivalent circuit parameters for the three antennas. The equivalent circuit parameters for an antenna of any scaling σ is then obtained by a quadratic interpolation of these parameters. (b) The quadratic approximation is then used to maximize the field enhancement at a desired frequency, e.g., at 200 GHz. The proposed circuit approach is subsequently employed to compute the field enhancement. The suggested circuit approach (solid line) is verified by computing the resized antenna by 3-D FEM (dashed) and excellent agreement of the two is found.

caution though, as we will see below. This decrease is mostly due to the fact that we are increasingly off resonant when increasing the modulator length. Lastly, it is also worth defining the figure of merit of a combined antenna-modulator system by:

$$\text{FOM} = \text{FE} \cdot l_{\text{mod}}. \quad (14)$$

This definition is motivated by the following [43], which shows that the optical phase shift $\Delta\varphi_{\text{opt}}$ of a phase modulator

given by

$$\Delta\varphi_{\text{opt}} = \frac{2\pi}{\lambda_{\text{opt}}} \Delta n_{\text{eff}}(E_m) l_{\text{mod}}, \quad (15)$$

with - assuming a linear refractive index change

$$\Delta n_{\text{eff}}(E_m) = \Gamma n_{\text{slow}} \frac{r}{2} n_{\text{mat}}^2 E_m. \quad (16)$$

This way, the FOM is proportional to the sensitivity $\Delta\varphi_{\text{opt}}/E_i$ of the antenna-modulator system. Equation (16) contains the material parameters n_{mat} , the linear refractive index and r , the electro-optic coefficient, as well as the energy interaction factor Γ and the surface-plasmon-polariton (SPP) slow-down factor n_{slow} , which have some geometry dependence, are neglected in this discussion. The FOM is plotted for different modulator geometries in Fig. 9(b). The plot indicates that the longest possible modulator has the highest FOM. However, these results should be interpreted with care: The actual FOM might be higher, as we have not yet optimized the circuit for operation at the highest FE value corresponding to a resonance at 200 GHz. Additionally, it is worth mentioning that careful consideration should be given to plasmonic losses. As the modulator length increases or the slot width decreases, the plasmonic losses are increasing.

On another note, as plasmonic modulator antennas comprise of a capacitive section, the well-known inverse relation between antenna scale and frequency of operation becomes invalid. The ideal length of the antenna is related to the modulator capacitance. In order to find the optimal antenna-modulator combination with the antenna resonance at the desired frequency, one has to match the antenna to the capacitance of the modulator. Starting from our analysis that covers coupled effects, a method is developed to design the best possible plasmonic modulator antenna for any frequency of operation, see Fig. 10(a).

Our aim is to find the ideal plasmonic modulator antennas that has a resonance at 200 GHz. Towards this goal, we select three representative antennas with resonance frequencies covering the desired range. Fig. 10(b) shows the antenna current-frequency response for three different scales σ of modulator antennas. The scaling factors of the three antennas are 0.50 (green line), 0.75 (red line), and 1.00 (blue line). Subsequently, the respective equivalent circuit values R_{ec} , C_{ec} , and L_{ec} (not only the antenna impedance, Z_a) for a fixed modulator (fixed capacitance and width) and the three antenna sizes are needed to be extracted. We then use these datasets to find the relation between parameters and the scaling. A quadratic approximation may be applied to find the resonance φ at a desired frequency. This way the fitting size for the resonance frequency at e.g., $f = 200$ GHz can be found. The field enhancement response of the approximated (scale factor σ of 0.692) structure is presented in Fig. 10(c). Again, we perform the FE calculations both with the circuit analysis (solid dark blue line) and the 3-D FEM (dashed light blue line). It can be clearly observed that both the circuit approximation and the 3-D-FEM responses are fitting well, and the relative error is computed as less than 5%. This allows us to achieve designing the best possible antenna for any desired frequency.

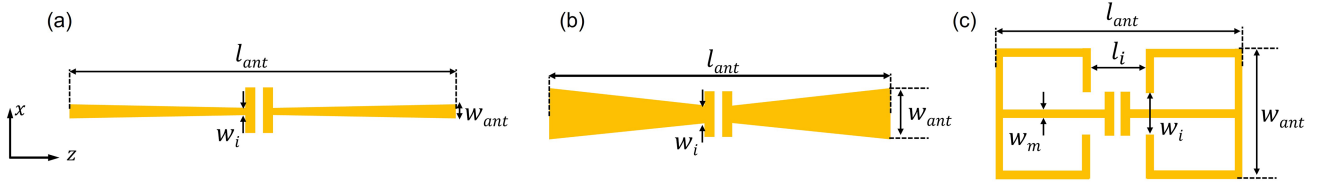


Fig. 11. Antenna types, (a) thin bowtie, (b) wide bowtie, and (c) FLC, which are commonly used in combination with plasmonic modulators are investigated.

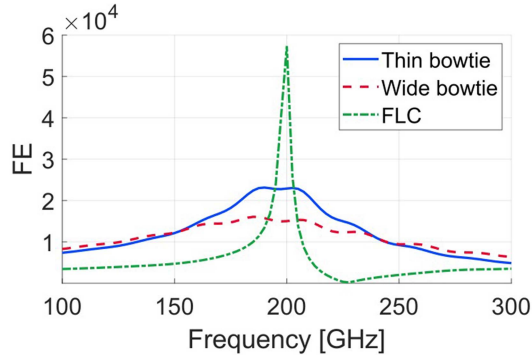


Fig. 12. Field enhancement responses of the thin bowtie, the wide bowtie, and the FLC with respect to frequency is given.

V. DISCUSSION OF PLASMONIC ANTENNAS AND THE GEOMETRY WITH THE HIGHEST FIELD ENHANCEMENT

Following, we apply the proposed method on some realistic plasmonic modulator antenna designs. The field enhancement behavior of different antennas will be analyzed. Additionally, we apply the framework based on our proposed method to obtain the equivalent circuit parameters.

We now introduce three different planar THz antenna types, see Fig. 11. This includes the thin bowtie, the wide bowtie, and the four-leaf clover (FLC) antennas [11] for co-integration with the plasmonic modulator. The bowtie geometry comes with three different design parameters: the length of the antenna (l_{ant}), and the inner and outer widths of the antenna (w_i and w_{ant}), respectively [10]. For the thin bowtie antenna, the parameters are selected as $l_{ant} = 1.196$ mm, $w_{ant} = 18.38$ μm , and $w_i = 2.94$ μm , while, for the wide bowtie antenna; $l_{ant} = 1.118$ mm, $w_{ant} = 258$ μm , and $w_i = 3.04$ μm . The FLC parameters are given as $l_{ant} = 0.615$ mm, $w_{ant} = 0.224$ mm, $l_i = 93.93$ μm , $w_i = 23.96$ μm , and $w_m = 22.95$ μm . The modulator section is designed with $w_{mod} = 4$ μm , $l_{mod} = 14$ μm , and $w_{slot} = 0.1$ μm . All the structures are modeled with a thickness of $d_{mod} = 0.1$ μm . The plasmonic modulators with the antennas are designed for the frequency 200 GHz. The plane wave excitation propagates in the y -direction and the polarization of the incident field is aligned along the z -axis. Its field is $E_i = 5$ V/m.

Following the proposed theory that was explained thoroughly in the previous section, the equivalent circuit parameters are obtained for the above-mentioned antenna designs as listed in Table III.

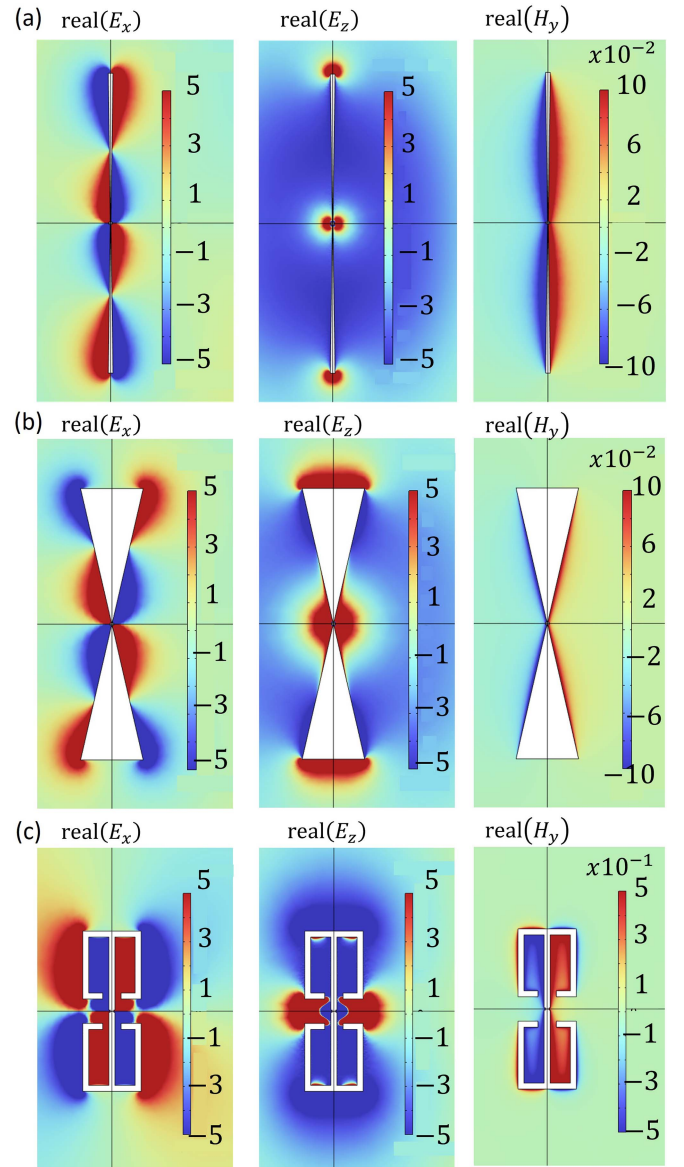


Fig. 13. Corresponding near electric and magnetic field plots of the structure, (a) thin bowtie, (b) wide bowtie, and (c) FLC are shown. For modulation, the E_z -field within the slot has to be maximized.

As seen from Fig. 12, these three antennas vary in their field enhancement responses; thereby, they are employed for different applications (i.e., the FLC for the highest field enhancement and narrowband operation, the bowtie for broadband operation, etc.). To obtain an understanding of the field enhancement values, the

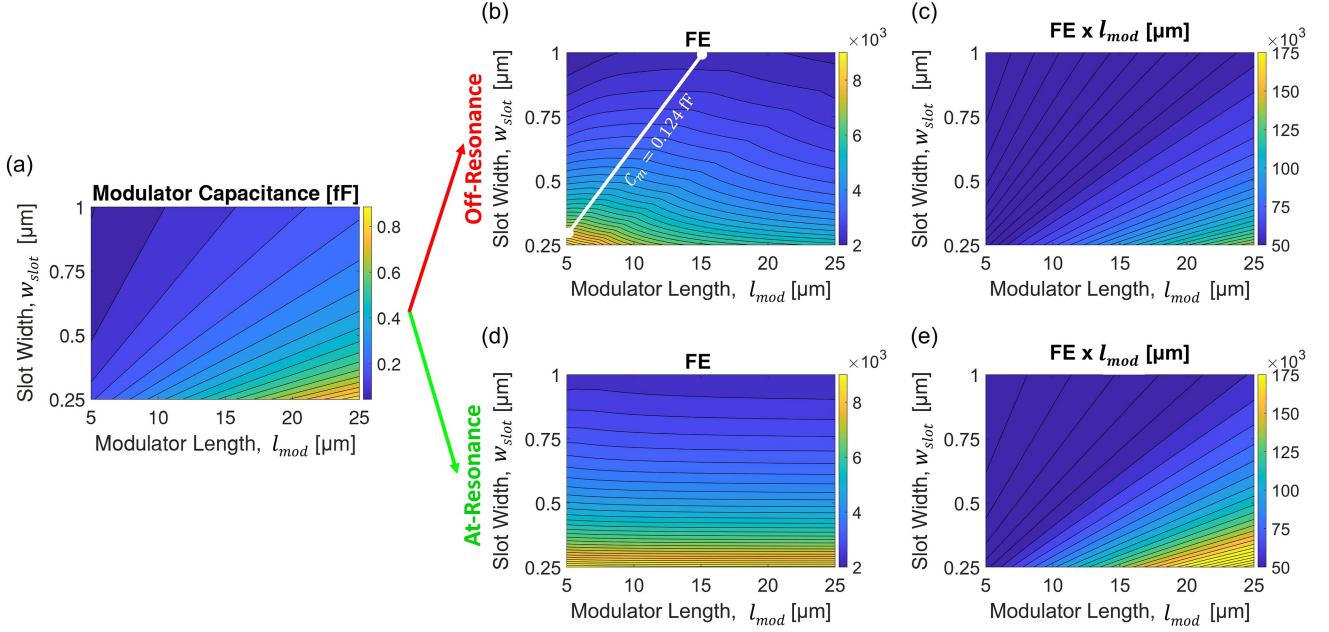


Fig. 14. For the given thin bowtie antenna, the FE and FOM responses with changing modulator dimensions are investigated at two distinct cases: At resonance and off-resonance. (a) Search space of modulator capacitances for both at-resonance and off-resonance cases are given. (b)–(c) For the off-resonance case, the FE and FOM responses are shown. (d)–(e) FE and FOM responses of the at-resonance case are demonstrated.

TABLE III
EQUIVALENT CIRCUIT PARAMETERS OF DIFFERENT ANTENNAS
WITH MODULATOR

PARAMETER	THIN BOWTIE	WIDE BOWTIE	FLC	UNIT
I_a	7.91	9.53	4.777	μA
U_g	14.74	13.034	11.999	mV
Z_g	376.8	376.82	376.82	Ω
U_a	11.79	9.655	10.364	mV
C_{ec}	0.007	0.21058	0.01055	fF
R_{ec}	137.34	28.755	6405.31	k Ω
L_{ec}	8.01	2.9362	62.6908	nH
C_m	2.357	7.9039	0.1391	fF
U_m	2.669	0.9595	27.318	mV
FE	22860	15020	58600	

voltage value across the modulator can provide insight. For that matter, a comparison of voltage U_m values across the modulator shows that the FLC antenna provides the highest maximum field enhancement values while the wide bowtie has the lowest one, see Table III. Similarly, the value of the equivalent resistance R_{ec} also affects the ability of the antenna to radiate/capture electromagnetic field; hence, the field enhancement behavior.

The comparison of the calculated circuit parameters of the aforementioned antennas can reveal additional information: The wider the antenna width, the higher the equivalent antenna capacitance, C_{ec} . As expected, the equivalent antenna inductance, L_{ec} , is highest for the FLC antenna due to its loop-like design.

Fig. 13 shows the near-field electric and magnetic field distributions over these antennas. All three types have the electric

field intensity maximum occurring at the antenna slot, where the plasmonic modulator is located. The magnetic field has a local minimum but does not drop to zero at the slot (since the current is non-zero between the capacitor plates of the modulator). Also, at the antenna arm ends, the local electric field maxima and magnetic field minima are observed (analogy with open circuit termination). The field plots of the thin bowtie in Fig. 13(a), and the wide bowtie in Fig. 13(b), have a similar trend. For the wide bowtie antenna, it is observed that the electric field is spreading into a larger area rather than localizing (as in the thin bowtie case) since it is covering more area in space. The reverse effect is observed for the magnetic field plots. The loop like geometrical shape of FLC leads to a different field distribution. As in Fig. 13(c), it has this alternating field response at the opposite sides of the antenna arms. The maxima and minima locations also follow the theory for both electric and magnetic field distributions. Since the antenna ends meet at the antenna slot, the electric field maximum is found in the center of the structure. In a similar way, the magnetic field is only close to zero in the middle of the structure.

Lastly, we are aiming to find the antenna that induces the largest phase shift. The question then is as of which antenna provides the best $\text{FOM} = \text{FE} \cdot l_{mod}$. Towards this end, we choose the thin bowtie antenna, and we investigate the space encompassing different modulator lengths and modulator slot widths. This results in a capacitance plot as depicted in Fig. 14(a). Subsequently, we try find the optimum plasmonic antenna in two ways:

In a first attempt, we study the modulator with the thin bowtie antenna and the antenna geometry that led to the parameters in Table III. This antenna has a resonance at 200 GHz for a modulator with slot width $w_{slot} = 0.1 \mu\text{m}$ and a length

$l_{mod} = 14 \mu\text{m}$ (capacitance $C_m = 0.124 \text{ fF}$). When varying the modulator geometry, we obtain the FE plot from Fig. 14(b). For a given modulator slot width w_{slot} one may find a maximum FE at a specific length l_{mod} . Yet, this is not the global maximum. By following the capacitance equiline (white line) towards smaller slot widths (i.e., by staying at resonance) we can increase the field enhancement. All of this is achieved with the same antenna geometry. It should be noted that, in the end, what matters is the FE l_{mod} . The plot in Fig. 14(c) then shows that increasing the length has still more impact. Increasing the modulator length can indeed enhance the figure of merit.

In a second attempt, for each modulator capacitance (i.e., each slot width w_{slot} and length l_{mod} of the modulator), we redesign a new optimum resonant antenna. The antenna with a resonance at 200 GHz for any of the modulator capacitances. This process results in the FE plots of Fig. 14(d). These resonant antennas provide the same FE at any modulator length! This is quite an amazing result as the charges fed to the modulator need to increase in order to maintain the same FE for all lengths. This can be understood as follows: The antenna rescaling redistributes the charges from the antenna to the modulator. When subsequently multiplying the FE by the length, one obtains the figure of merit in the plot of Fig. 14(e). As a result, we can find the antenna with the highest figure of merit by studying the plot. Again, the highest phase shift is found for the longer antennas. The length of the antenna thus should be as long as possible – yet not too long or the plasmonic losses might become prohibitively high.

VI. CONCLUSION

In this article, a framework for designing plasmonic modulator antennas is presented. The method is based on the antenna equivalent circuit theory and extracting its individual components through computational analysis. This evaluation is performed via field simulations as opposed to the use of lumped port excitation, which has been found inadequate in revealing the influence of the modulator on the antenna. Our proposed method is thus introduced as a more accurate means of modeling the plasmonic modulator antenna.

The comparison between half-wavelength dipole and full-wavelength dipole with plasmonic modulator shows the impact of this co-integration. Their equivalent circuit parameters and field plots are analyzed in detail to explain the effects of each design part on the performance. Furthermore, three different structures that are used with plasmonic modulator antenna applications, namely thin bowtie, wide bowtie, and FLC are further analyzed. The circuit approach shed light on the field enhancement behavior of these structures in terms of their bandwidth and enhancement capabilities.

The fractional bandwidth of these plasmonic antenna is not only impacted by the antenna geometry, but also highly influenced by the plasmonic modulator. Yet, the proposed method can be utilized to design the best possible plasmonic antenna for any frequency. The framework offers an efficient way based on theory rather than performing many parameter sweeps for finding an aimed field enhancement response despite the fact that all design parameters are coupled.

While this article gives insights into the physics of the antenna modulator, it should be stressed that for a practical implementation one has to include not only substrates and cladding materials but also reflections at interfaces.

APPENDIX

A. Lumped Port Excitation

The details of the lumped excitation is explained in this Appendix. As discussed previously, the lumped port is connected to a source with a generator voltage U_g and a generator impedance of R_g . The voltage U_p is induced across the port with a port current of I_p . The generator voltage U_g excites an incident field with an electric field component of E_i and a magnetic field component of H_i . At the lumped port, the scattered field with an electric field component of E_{ref} and a magnetic field component of H_{ref} also radiates. The transmission line current is also represented as a surface current density J_s with an opposite direction to the electric field. The lumped port details are given in Fig. 15.

The incident and reflected electric and magnetic fields are related through the surface impedance as follows

$$\vec{n} \times \vec{H}_i = -\frac{1}{Z_s} \vec{n} \times (\vec{n} \times \vec{E}_i) \quad (17)$$

$$\vec{n} \times \vec{H}_{ref} = \frac{1}{Z_s} \vec{n} \times (\vec{n} \times \vec{E}_{ref}). \quad (18)$$

Summing (16) and (17) results in the following equation.

$$\vec{n} \times (\vec{H}_i + \vec{H}_{ref}) = \frac{1}{Z_s} \vec{n} \times [\vec{n} \times (\vec{E}_{ref} - \vec{E}_i)] \quad (19)$$

$$\vec{n} \times \left(\underbrace{\vec{H}_i + \vec{H}_{ref}}_{\vec{H}} \right) = \frac{1}{Z_s} \vec{n} \times \left[\vec{n} \times \left(\underbrace{\vec{E}_{ref} + \vec{E}_i}_{\vec{E}} - 2\vec{E}_i \right) \right] \quad (20)$$

$$\vec{n} \times \vec{H} = \frac{1}{Z_s} \vec{n} \times (\vec{n} \times \vec{E}) - \frac{2}{Z_s} \vec{n} \times (\vec{n} \times \vec{E}_i). \quad (21)$$

In order to obtain the boundary condition defined over electric field, the derivative of (21) is taken.

$$\vec{n} \times \left[\frac{1}{\mu} \left(\mu \frac{\partial \vec{H}}{\partial t} \right) \right] = \frac{1}{Z_s} \vec{n} \times \left(\vec{n} \times \frac{\partial \vec{E}}{\partial t} \right) - \frac{2}{Z_s} \vec{n} \times \left(\vec{n} \times \frac{\partial \vec{E}_i}{\partial t} \right) \quad (22)$$

The first Maxwell's equation, $\nabla \times \vec{E} = -\mu \frac{\partial \vec{H}}{\partial t}$, is then utilized to reach the final form of the boundary condition.

$$\vec{n} \times \left(\frac{1}{\mu} \nabla \times \vec{E} \right) = -\frac{1}{Z_s} \vec{n} \times \left(\vec{n} \times \frac{\partial \vec{E}}{\partial t} \right) + \frac{2}{Z_s} \vec{n} \times \left(\vec{n} \times \frac{\partial \vec{E}_i}{\partial t} \right) \quad (23)$$

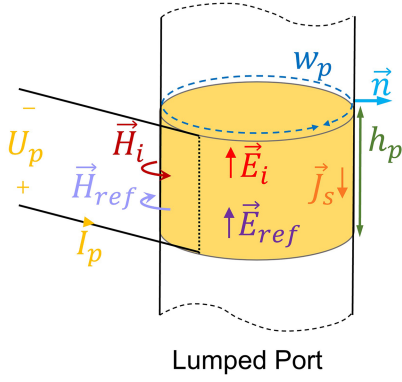


Fig. 15. Simple lumped port representation is illustrated. The source generates the port voltage U_p and the port current I_p at the lumped port. As a result of this excitation, the incident field with an electric field component of E_i and a magnetic field component of H_i is induced. The scattered field at the lumped port has an electric field component of E_{ref} and a magnetic field component of H_{ref} . The port has a height h_p and a circumference w_p . The transmission line current is also represented as a surface current density J_s with an opposite direction to the electric field. More details can be found in the text.

$$\begin{aligned} \vec{n} \times \left(\frac{1}{\mu} \nabla \times \vec{E} \right) + \frac{1}{Z_s} \vec{n} \times \left(\vec{n} \times \frac{\partial \vec{E}}{\partial t} \right) \\ = \frac{2}{Z_s} \vec{n} \times \left(\vec{n} \times \frac{\partial \vec{E}_i}{\partial t} \right). \end{aligned} \quad (24)$$

B. Equivalent Circuit Parameter Derivation

The details of the derivation of the equivalent circuit model parameters from the computed values is explained in this Appendix.

As illustrated in Fig. 3, 3-D FEM simulations are performed to obtain the antenna current (I_a), the scattered power from the antenna (P_r) over the surface of the air domain, and the time-average electric (W_e) and magnetic (W_m) energies of the scattered field in the air domain. Hereafter, the decomposition of the radiating and near-field parts of the time-average energies are obtained as expressed by (5)–(7). The time-average electric energy of the near-field (W_e^{near}) and the time-average magnetic energy of the near-field (W_m^{near}) are then required for computing the antenna capacitance (C_{ec}), the inductance values (L_{ec}) and the antenna resistance (R_{ec}).

The value of the antenna capacitance C_{ec} can be derived from the electric energy of the near-field (W_e^{near}) by using

$$W_e^{near} = \frac{1}{2} C_{ec} U_{C_{ec}}^2, \quad (25)$$

where $U_{C_{ec}}$ is the voltage across the antenna capacitance

$$U_{C_{ec}} = \frac{I_a}{j\omega C_{ec}}. \quad (26)$$

Solving (25) with (26) for C_{ec} gives

$$C_{ec} = \frac{I_a^2}{2\omega^2 W_e^{near}}. \quad (27)$$

The remaining equivalent circuit parameters, namely antenna inductance (L_{ec}) and antenna resistance (R_{ec}) are extracted by utilizing the computed values, as well as Kirchhoff's circuit laws.

We first use the Kirchhoff's law to derive the currents I_r and I_l flowing in the circuit of Fig. 3. Kirchhoff yields the following equations

$$I_r R_{ec} - j\omega L_{ec} I_l = 0, \quad (28)$$

$$I_a = I_r + I_l. \quad (29)$$

By inserting (29) into (28), the current I_r flowing through the antenna resistance can be found as follows

$$I_r = \frac{j\omega L_{ec} I_l}{R_{ec}} = \frac{j\omega L_{ec} (I_a - I_r)}{R_{ec}}. \quad (30)$$

and solving (30) for I_r yields

$$I_r = \frac{j\omega L_{ec}}{R_{ec} + j\omega L_{ec}} I_a. \quad (31)$$

Similarly, the current flowing through the antenna inductance can be obtained by using (29) and (31) as

$$I_l = \frac{R_{ec}}{R_{ec} + j\omega L_{ec}} I_a. \quad (32)$$

The power radiated from the antenna (P_r) is equal to the power consumed by the antenna resistance ($P_{R_{ec}}$)

$$P_r = P_{R_{ec}} = \frac{1}{2} R_{ec} I_r^2. \quad (33)$$

The time-average near-field magnetic energy is given by

$$W_m^{near} = \frac{1}{2} L_{ec} I_l^2. \quad (34)$$

The power radiated by the antenna and the time-average near-field magnetic energy given in (33) and (34) can be written in the following form by inserting the current expressions into (31) and (32), respectively.

$$P_r = \frac{1}{2} R_{ec} I_r^2 = \frac{1}{2} R_{ec} \frac{\omega^2 L_{ec}^2}{R_{ec}^2 + \omega^2 L_{ec}^2} I_a^2, \quad (35)$$

$$W_m^{near} = \frac{1}{2} L_{ec} I_l^2 = \frac{1}{2} L_{ec} \frac{R_{ec}^2}{R_{ec}^2 + \omega^2 L_{ec}^2} I_a^2. \quad (36)$$

To extract the antenna resistance and the antenna inductances from (33) and (34), (35) and (36) can be combined as follows

$$P_r^2 + \omega^2 W_m^{near2} = \frac{1}{4} \frac{\omega^2 R_{ec}^2 L_{ec}^2}{R_{ec}^2 + \omega^2 L_{ec}^2} I_a^4. \quad (37)$$

Using (37) with (35) and (36), respectively, allows one to extract the two values

$$R_{ec} = \frac{2(P_r^2 + \omega^2 W_m^{near2})}{P_r I_a^2} \quad \text{and} \quad (38)$$

$$L_{ec} = \frac{2(P_r^2 + \omega^2 W_m^{near2})}{\omega^2 W_m^{near} I_a^2} = R_{ec} \frac{P_r}{\omega^2 W_m^{near}}. \quad (39)$$

The rest of the parameters such as source voltage, U_g and antenna voltage, U_a are calculated by using Ohm's law.

REFERENCES

- [1] W. B. Bridges, F. T. Sheehy, and J. H. Schaffner, "Wave-coupled LiNbO₃/sub 3/electrooptic modulator for microwave and millimeter-wave modulation," *IEEE Photon. Technol. Lett.*, vol. 3, no. 2, pp. 133–135, Feb. 1991, doi: [10.1109/68.76865](https://doi.org/10.1109/68.76865).
- [2] D. Marpaung, J. Yao, and J. Capmany, "Integrated microwave photonics," *Nature Photon.*, vol. 13, no. 2, pp. 80–90, Feb. 2019, doi: [10.1038/s41566-018-0310-5](https://doi.org/10.1038/s41566-018-0310-5).
- [3] R. A. Minasian, "Photonic signal processing of microwave signals," *IEEE Trans. Microw. Theory Techn.*, vol. 54, no. 2, pp. 832–846, Feb. 2006, doi: [10.1109/TMTT.2005.863060](https://doi.org/10.1109/TMTT.2005.863060).
- [4] Y. N. Wijayanto, H. Murata, and Y. Okamura, "Novel electro-optic microwave-lightwave converters utilizing a patch antenna embedded with a narrow gap," *Inst. Elect. Electron. Engineers Electron. Exp.*, vol. 8, no. 7, pp. 491–497, 2011, doi: [10.1587/elex.8.491](https://doi.org/10.1587/elex.8.491).
- [5] X. Zhang et al., "Integrated photonic electromagnetic field sensor based on broadband bowtie antenna coupled silicon organic hybrid modulator," *J. Lightw. Technol.*, vol. 32, no. 20, pp. 3774–3784, Oct. 2014, doi: [10.1109/JLT.2014.2319152](https://doi.org/10.1109/JLT.2014.2319152).
- [6] O. D. Herrera et al., "Silica/electro-optic polymer optical modulator with integrated antenna for microwave receiving," *J. Lightw. Technol.*, vol. 32, no. 20, pp. 3861–3867, Oct. 2014, doi: [10.1109/JLT.2014.2316672](https://doi.org/10.1109/JLT.2014.2316672).
- [7] D. H. Park et al., "Free space millimeter wave-coupled electro-optic high speed nonlinear polymer phase modulator with in-plane slotted patch antennas," *Opt. Exp.*, vol. 23, no. 7, pp. 9464–9476, Apr. 2015, doi: [10.1364/OE.23.009464](https://doi.org/10.1364/OE.23.009464).
- [8] K. A. Abdalmalak et al., "Microwave radiation coupling into a WGM resonator for a high-photonics-efficiency nonlinear receiver," in *Proc. IEEE 48th Eur. Microw. Conf.*, 2018, pp. 781–784, doi: [10.23919/EuMC.2018.8541628](https://doi.org/10.23919/EuMC.2018.8541628).
- [9] A. Dawoud and K. Atia, "Analysis and design of antennas and radiometers for radio astronomy applications in microwave, Mm-wave, and THz Bands," 2022. Accessed: Aug. 31, 2023. [Online]. Available: <https://e-archivo.uc3m.es/handle/10016/35126>
- [10] Y. Salamin et al., "Direct conversion of free space millimeter waves to optical domain by plasmonic modulator antenna," *Nano Lett.*, vol. 15, no. 12, pp. 8342–8346, Dec. 2015, doi: [10.1021/acs.nanolett.5b04025](https://doi.org/10.1021/acs.nanolett.5b04025).
- [11] Y. Salamin et al., "Compact and ultra-efficient broadband plasmonic terahertz field detector," *Nature Commun.*, vol. 10, no. 1, Dec. 2019, Art. no. 5550, doi: [10.1038/s41467-019-13490-x](https://doi.org/10.1038/s41467-019-13490-x).
- [12] Y. Salamin et al., "Microwave plasmonic mixer in a transparent fibre-wireless link," *Nature Photon.*, vol. 12, no. 12, pp. 749–753, Dec. 2018, doi: [10.1038/s41566-018-0281-6](https://doi.org/10.1038/s41566-018-0281-6).
- [13] C. A. Balanis, *Antenna Theory: Analysis and Design*. Hoboken, NJ, USA: Wiley, 2005.
- [14] Y. He, Y. Chen, L. Zhang, S.-W. Wong, and Z. N. Chen, "An overview of terahertz antennas," *China Commun.*, vol. 17, no. 7, pp. 124–165, Jul. 2020, doi: [10.23919/JCC.2020.07.011](https://doi.org/10.23919/JCC.2020.07.011).
- [15] T. G. Tang, Q. M. Tieng, and M. W. Gunn, "Equivalent circuit of a dipole antenna using frequency-independent lumped elements," *IEEE Trans. Antennas Propag.*, vol. 41, no. 1, pp. 100–103, Jan. 1993, doi: [10.1109/8.210122](https://doi.org/10.1109/8.210122).
- [16] M. Hamid and R. Hamid, "Equivalent circuit of dipole antenna of arbitrary length," *IEEE Trans. Antennas Propag.*, vol. 45, no. 11, pp. 1695–1696, Nov. 1997, doi: [10.1109/8.650083](https://doi.org/10.1109/8.650083).
- [17] S. R. Best and B. C. Kaanta, "A tutorial on the receiving and scattering properties of antennas," *IEEE Antennas Propag. Mag.*, vol. 51, no. 5, pp. 26–37, Oct. 2009, doi: [10.1109/MAP.2009.5432036](https://doi.org/10.1109/MAP.2009.5432036).
- [18] J. J. Adams and J. T. Bernhard, "Broadband equivalent circuit models for antenna impedances and fields using characteristic modes," *IEEE Trans. Antennas Propag.*, vol. 61, no. 8, pp. 3985–3994, Aug. 2013, doi: [10.1109/TAP.2013.2261852](https://doi.org/10.1109/TAP.2013.2261852).
- [19] F. Sadeghikia, "Analysis of plasma monopole antenna using numerical method and an equivalent circuit," *IEEE Antennas Wireless Propag. Lett.*, vol. 16, pp. 1711–1714, 2017, doi: [10.1109/LAWP.2017.2669091](https://doi.org/10.1109/LAWP.2017.2669091).
- [20] F. Mokhtari-Koushyar et al., "Wideband multi-arm bowtie antenna for millimeter wave electro-optic sensors and receivers," *J. Lightw. Technol.*, vol. 36, no. 16, pp. 3418–3426, Aug. 2018, doi: [10.1109/JLT.2018.2842712](https://doi.org/10.1109/JLT.2018.2842712).
- [21] J. R. Bray, "An improved antenna scattering model: An equivalent model based on the reciprocity theorem," *IEEE Antennas Propag. Mag.*, vol. 61, no. 4, pp. 30–38, Aug. 2019, doi: [10.1109/MAP.2019.2920066](https://doi.org/10.1109/MAP.2019.2920066).
- [22] B. Sievert et al., "Equivalent circuit model separating dissipative and radiative losses for the systematic design of efficient microstrip-based on-chip antennas," *IEEE Trans. Microw. Theory Techn.*, vol. 69, no. 2, pp. 1282–1294, Feb. 2021, doi: [10.1109/TMTT.2020.3040453](https://doi.org/10.1109/TMTT.2020.3040453).
- [23] Y. N. Wijayanto, A. A. Fathnan, A. Kanno, D. Mahmudin, and P. Daud, "Metamaterial antenna on electro-optic modulator for wireless Terra-Hertz detection through radio-over-fibre technology," in *Proc. Inst. Phys. Conf. Ser. Mater. Sci. Eng.*, 2019, Art. no. 012004, doi: [10.1088/1757-899X/622/1/012004](https://doi.org/10.1088/1757-899X/622/1/012004).
- [24] H. Murata, "Millimeter-wave-band electro-optic modulators using antenna-coupled electrodes for microwave photonic applications," *J. Lightw. Technol.*, vol. 38, no. 19, pp. 5485–5491, Oct. 2020, doi: [10.1109/JLT.2020.3004176](https://doi.org/10.1109/JLT.2020.3004176).
- [25] T. Kaji et al., "W-band optical modulators using electro-optic polymer waveguides and patch antenna arrays," *Opt. Exp.*, vol. 29, no. 19, pp. 29604–29614, Sep. 2021, doi: [10.1364/OE.434028](https://doi.org/10.1364/OE.434028).
- [26] H. Lu, Y. Li, and J. Zhang, "Design and analysis of broadband LiNbO₃ optical waveguide electric field sensor with tapered antenna," *Sensors*, vol. 21, no. 11, Jan. 2021, Art. no. 3672, doi: [10.3390/s21113672](https://doi.org/10.3390/s21113672).
- [27] H. Ibili, A. C. Gungor, M. Maciejewski, J. Smajic, and J. Leuthold, "Genetic algorithm based geometry optimization of Terahertz plasmonic modulator antennas," in *Proc. IEEE 23rd Int. Conf. Computation Electromagn. Fields*, 2022, pp. 1–4, doi: [10.1109/COMPUMAG55718.2022.9827512](https://doi.org/10.1109/COMPUMAG55718.2022.9827512).
- [28] M. Burla et al., "500 GHz plasmonic Mach-Zehnder modulator enabling sub-THz microwave photonics," *Appl. Phys. Lett. Photon.*, vol. 4, no. 5, May 2019, Art. no. 056106, doi: [10.1063/1.5086868](https://doi.org/10.1063/1.5086868).
- [29] Y. Horst et al., "Transparent optical-THz-optical link at 240/192 Gbit/s Over 5/115 m enabled by plasmonics," *J. Lightw. Technol.*, vol. 40, no. 6, pp. 1690–1697, Mar. 2022.
- [30] P. Ma et al., "Low-Loss Plasmonically Enhanced Graphene-Organic Hybrid Phase Modulator with >270 GHz Modulation Bandwidth," in *Proc. Eur. Conf. Opt. Commun.*, 2022, Paper Th3B.4.
- [31] A. Melikyan et al., "High-speed plasmonic phase modulators," *Nature Photon.*, vol. 8, no. 3, pp. 229–233, Mar. 2014, doi: [10.1038/nphoton.2014.9](https://doi.org/10.1038/nphoton.2014.9).
- [32] C. Haffner et al., "All-plasmonic Mach-Zehnder modulator enabling optical high-speed communication at the microscale," *Nature Photon.*, vol. 9, no. 8, pp. 525–528, Aug. 2015, doi: [10.1038/nphoton.2015.127](https://doi.org/10.1038/nphoton.2015.127).
- [33] A. Messner et al., "Plasmonic ferroelectric modulators," *J. Lightw. Technol.*, vol. 37, no. 2, pp. 281–290, Jan. 2019, doi: [10.1109/JLT.2018.2881332](https://doi.org/10.1109/JLT.2018.2881332).
- [34] B. H. Robinson et al., "Optimization of plasmonic-organic hybrid electro-optics," *J. Lightw. Technol.*, vol. 36, no. 21, pp. 5036–5047, Nov. 2018, doi: [10.1109/JLT.2018.2865882](https://doi.org/10.1109/JLT.2018.2865882).
- [35] Y. Salamin et al., "Antenna coupled plasmonic modulator," in *Proc. Front. Opt.*, 2015, Paper FTh1B.5, doi: [10.1364/FIO.2015.FTh1B.5](https://doi.org/10.1364/FIO.2015.FTh1B.5).
- [36] K. Tekkouk et al., "Corporate-feed slotted waveguide array antenna in the 350-GHz band by silicon process," *IEEE Trans. Antennas Propag.*, vol. 65, no. 1, pp. 217–225, Jul. 2017, doi: [10.1109/TAP.2016.2631132](https://doi.org/10.1109/TAP.2016.2631132).
- [37] K. Fan, Z.-C. Hao, Q. Yuan, and W. Hong, "Development of a high gain 325–500 GHz antenna using quasi-planar reflectors," *IEEE Trans. Antennas Propag.*, vol. 65, no. 7, pp. 3384–3391, Jul. 2017, doi: [10.1109/TAP.2017.2705022](https://doi.org/10.1109/TAP.2017.2705022).
- [38] A. Gomez-Torrent et al., "A 38 dB gain, low-loss, flat array antenna for 320–400 GHz enabled by silicon-on-insulator micromachining," *IEEE Trans. Antennas Propag.*, vol. 68, no. 6, pp. 4450–4458, Jun. 2020, doi: [10.1109/TAP.2020.2969753](https://doi.org/10.1109/TAP.2020.2969753).
- [39] F. F. Manzanillo, A. Clemente, and J. L. González-Jiménez, "High-gain D-band transmitarrays in standard PCB technology for beyond-5G communications," *IEEE Trans. Antennas Propag.*, vol. 68, no. 1, pp. 587–592, Jan. 2020, doi: [10.1109/TAP.2019.2938630](https://doi.org/10.1109/TAP.2019.2938630).
- [40] B. Aqlan, M. Himdi, H. Vettikalladi, and L. Le-Coq, "A 300-GHz low-cost high-gain fully metallic Fabry-Perot cavity antenna for 6G terahertz wireless communications," *Sci. Rep.*, vol. 11, no. 1, Apr. 2021, Art. no. 7703, doi: [10.1038/s41598-021-87076-3](https://doi.org/10.1038/s41598-021-87076-3).
- [41] C. A. Balanis, "Finite-element analysis and modeling of antennas," in *Modern Antenna Handbook*. Hoboken, NJ, USA: Wiley, 2008, pp. 1531–1593, doi: [10.1002/9780470294154.ch31](https://doi.org/10.1002/9780470294154.ch31).
- [42] S. D. Assimonis, M. A. B. Abbasi, and V. Fusco, "Millimeter-wave multi-mode circular antenna array for uni-cast multi-cast and OAM communication," *Sci. Rep.*, vol. 11, no. 1, Mar. 2021, Art. no. 4928, doi: [10.1038/s41598-021-83301-1](https://doi.org/10.1038/s41598-021-83301-1).
- [43] C. Haffner et al., "Plasmonic organic hybrid modulators—Scaling highest speed photonics to the microscale," *Proc. IEEE*, vol. 104, no. 12, pp. 2362–2379, Dec. 2016, doi: [10.1109/JPROC.2016.2547990](https://doi.org/10.1109/JPROC.2016.2547990).

Hande Ibili (Graduate Student Member, IEEE) received the B.Sc. and M.Sc. degrees in electrical and electronics engineering from Middle East Technical University, Ankara, Turkey, in 2016 and 2019, respectively. She is currently working toward the Ph.D. degree with the Institute of Electromagnetic Fields, ETH Zurich. Her research interests include plasmonic antennas, high-frequency electromagnetic field simulations, and THz communication.

Tobias Blatter is currently working toward the Ph.D. degree with the ETH Zurich's Institute of Electromagnetic Fields, Zurich, Switzerland lead by Professor J. Leuthold. His research interests include electro-optical modulators and THz-communication.

Michael Baumann received the M.Sc. degree in electrical engineering and information technology from ETH Zürich, Zürich, Switzerland, in 2018. In continuation of his master thesis with the Institute of Electromagnetic Fields at ETH, he joined the Institute as a Ph.D. student in the same year to work on high-speed plasmonic detectors. His research interests include integrated optics and nonlinear optics in silicon photonics, microwave photonics, and THz technology.

Laurenz Kulmer received the B.Sc. and M.Sc. degrees in electrical engineering and information technology in 2019 and 2021, respectively, from ETH Zurich, Zurich, Switzerland, where he is currently working toward the Ph.D. degree with the Institute of Electromagnetic Fields, Zurich, Switzerland. His research interests include optical communication, subTHz communication systems, and subTHz sensing systems.

Boris Vukovic received the M.S. degree in electrical engineering from ETH Zurich, Zurich, Switzerland, with the focus in electronics and photonics, where he is currently working toward the Ph.D. degree with the Institute of Electromagnetic Fields, Zurich, Switzerland. His main research interests include being THz communication and integrated photonic THz devices.

Jasmin Smajic (Senior Member, IEEE) received the B.Sc. degree from the Faculty of Electrical Engineering in Tuzla, Bosnia and Herzegovina, in 1996, and the M.Sc. and Ph.D. degrees from the Faculty of Electrical Engineering and Computing, Zagreb, Croatia, in 1998 and 2001, respectively, on the topic of numerical computing and optimization of static and time-varying electromagnetic fields. After his Postdoctoral Research with the ETH Zurich from 2002 to 2004 on the topic of full-Maxwell electromagnetic simulations of photonic crystals, he took a position of scientist with the ABB Corporate Research Centre, Baden-Dättwil, Switzerland, where he stayed till 2011. His work in ABB covered a wide range of projects in the field of computational and applied electromagnetics. From 2011 to 2020, he was a Full Professor of electrical engineering with the University of Applied Sciences, Rapperswil, Switzerland, where he was leading Computational and Applied Electromagnetics Group. Since 2020, he has been a Senior Scientist with the Swiss Federal Institute of Technology, ETH, Zurich, Switzerland. He has authored more than hundred scientific publications, several books, and dozens of patents. He is also a Member of CIGRE.

Juerg Leuthold (Fellow, IEEE) received the Ph.D. degree in physics from ETH Zürich, Zürich, Switzerland, in 1998, for work in the field of integrated optics and all-optical communications. Since 2013, he has been the Head of the Institute of Electromagnetic Fields, ETH Zurich, Zurich, Switzerland. From 2004 to 2013, he was with the Karlsruhe Institute of Technology, Karlsruhe, Germany, where he was the Head of the Institute of Photonics and Quantum Electronics and the Helmholtz Institute of Microtechnology. From 1999 to 2004, he was with Bell Labs, Lucent Technologies, Holmdel, NJ, USA, where he performed device and system research with III/V semiconductor and silicon optical bench materials for applications in high-speed telecommunications. His research interests include photonics, plasmonics, and microwave with an emphasis on applications in communications and sensing. Dr. Leuthold is a Fellow of the Optical Society of America and a Member of the Heidelberg Academy of Science. He was with the community as a Member of the Helmholtz Association Think Tank, Board of Directors of OSA, and in many technical program committees or as the General Chair of meetings.